

Two-dimensional numerical simulation of radio frequency sputter amorphous In–Ga–Zn–O thin-film transistors

Tze-Ching Fung,¹ Chiao-Shun Chuang,^{1,a)} Charlene Chen,¹ Katsumi Abe,² Robert Cottle,³ Mark Townsend,³ Hideya Kumomi,² and Jerzy Kanicki^{1,b)}

¹*Department of Electrical Engineering and Computer Science, University of Michigan, Ann Arbor, Michigan 48109, USA*

²*Canon Research Center, Canon Inc., 3-30-2 Shimomaruko, Ohta-ku, Tokyo 146-8501, Japan*

³*Silvaco International, Santa Clara, California 95054, USA*

(Received 25 June 2009; accepted 24 August 2009; published online 28 October 2009)

We reported on a two-dimensional simulation of electrical properties of the radio frequency (rf) sputter amorphous In–Ga–Zn–O (*a*-IGZO) thin-film transistors (TFTs). The *a*-IGZO TFT used in this work has the following performance: field-effect mobility (μ_{eff}) of $\sim 12 \text{ cm}^2/\text{V s}$, threshold voltage (V_{th}) of $\sim 1.15 \text{ V}$, subthreshold swing (S) of $\sim 0.13 \text{ V/dec}$, and on/off ratio over 10^{10} . To accurately simulate the measured transistor electrical properties, the density-of-states model is developed. The donorlike states are also proposed to be associated with the oxygen vacancy in *a*-IGZO. The experimental and calculated results show that the rf sputter *a*-IGZO TFT has a very sharp conduction band-tail slope distribution ($E_a = 13 \text{ meV}$) and Ti ohmic-like source/drain contacts with a specific contact resistance lower than $2.7 \times 10^{-3} \Omega \text{ cm}^2$. © 2009 American Institute of Physics. [doi:10.1063/1.3234400]

I. INTRODUCTION

During the past few years, there has been an increased interest in adapting amorphous In–Ga–Zn–O (*a*-IGZO) thin-film transistors (TFTs) as next generation TFT technology for flat-panel displays^{1,2} or photoimagers.^{3,4} Unlike covalent bond semiconductors (e.g., Si), the conduction band of In–Ga–Zn–O primarily depends on the overlap of heavy metal ion *ns* orbitals, which appears to be insensitive to the crystal distortion in the amorphous phase, leading to higher mobility materials.^{5–8} Today, *a*-IGZO used in TFTs is deposited by pulse laser deposition (PLD) or magnetron sputtering. Such device has a field-effect mobility ranging from 8 to 20 $\text{cm}^2/\text{V s}$, a subthreshold swing below 200 mV/dec, a threshold voltage (V_{th}) around 0 V, and an off current below $1 \times 10^{-12} \text{ A}$.^{9–12}

To understand the device physics and the TFT operation principles, the numerical simulation is an indispensable tool. However, despite the remarkable advances in device fabrication, there were only limited numbers of publications related to the numerical simulation of the *a*-IGZO TFT.^{13,14} The midgap density-of-state (DOS) models proposed for simulating *a*-IGZO electrical properties were fundamentally inherited from hydrogenated amorphous silicon (*a*-Si:H) with two components: the acceptorlike conduction band-tail states (g_{CBa}) and the acceptorlike deep-gap states (g_{Da}).¹⁵ In an earlier work, g_{CBa} and g_{Da} were considered to have the exponential and Gaussian distributions, respectively.¹³ After optimizing the numerical fit to the current-voltage (I/V) characteristics of the *a*-IGZO TFT, the characteristic energy slope (E_a) of g_{CBa} was determined to be 80 meV for the

enhancement mode device, while g_{Da} was observed to be very “flat,” without a clear peak structure.¹³ On the other hand, to simulate the electrical properties of the so called depletion mode TFT (negative threshold voltage), a shallower ($E_a = 140 \text{ meV}$) g_{CBa} and a larger g_{Da} were used.^{9,13} In addition, the band mobility used for depletion mode TFT simulation was set to a higher value; a possible generation of oxygen vacancy (OV) and an increase in carrier mobility (which is proportional to the carrier concentration) were given as justifications for this choice. The subsequent work proposed a simplified model by replacing the Gaussian distribution with the exponential distribution for g_{Da} .¹⁴ Model parameters were then extracted from the optical response of capacitance-voltage ($C-V$) characteristics of the *a*-IGZO TFT, and the characteristic energy slopes of g_{CBa} and g_{Da} determined by this method were 125 meV and 1.4 eV, respectively.¹⁴ Although two different mathematical formula were used to describe g_{Da} , both works project a low g_{Da} concentration $\sim 3 \times 10^{16} \text{ cm}^{-3} \text{ eV}^{-1}$ near the *a*-IGZO midgap ($E_C - E \sim 1.5 \text{ eV}$). Recently, a photofield-effect study conducted on the *a*-IGZO TFT also reveals a similar result, which suggested that the *a*-IGZO midgap DOS can be described by a linear distribution, and its value is an order lower than one reported for *a*-Si:H TFT.³

Even though the numerical simulation can achieve an adequate fit to the experimental I/V characteristics, our physical understanding of several *a*-IGZO properties is still rather poor. For example, so far E_a has been treated as a fitting parameter without any physical justification. It is well known that the broadened band-tail states originated from the long range structural disorder of amorphous semiconductors.¹⁶ Since the electron wave function is thought to experience minimum disturbance throughout the compound and the band conduction is still possible in *a*-IGZO,⁵ one would expect a much abrupt and sharper band

^{a)}Present affiliation: Diodes Inc., Hsinchu, Taiwan, R.O.C.

^{b)}Author to whom correspondence should be addressed. Electronic mail: kanicki@eecs.umich.edu.

edge for *a*-IGZO with E_a smaller or at least compatible to values obtained for *a*-Si:H (E_a for *a*-Si:H is ~ 25 meV).

The need to define different band mobilities for various types of *a*-IGZO TFTs also makes the simulation process very complex and, from device physics' point of view, unrealistic. It is known that due to the existence of band-tail states, only a portion of the total induced charges can participate in electrical conduction.¹⁷ As a result, TFT field-effect mobility is proportional to the total induced charge concentration (or gate voltage), and such effect has been studied in *a*-Si:H TFTs with numerical simulation.¹⁸ The band mobility used in numerical simulation should be kept as a constant unless the material structure is suspected to be seriously modified during device operation.

Finally, the nature of OV states should be carefully reviewed (i.e., donorlike or acceptorlike states). To maintain the electroneutrality of the compound, the OV states are "positively charged" rather than neutral when they are not filled by electrons. It is clearer when the defect equation for an OV is written in a Kröger–Vink notation as $V_O^{\times} \rightarrow V_O^{\bullet\bullet} + 2e'$.¹⁹ The above equation describes an OV acting as a donor and becomes doubly charged. The symbol V stands for vacancy, the subscript O represents the oxygen atom site, while the superscripts \times , \bullet , and $'$ represent neutral, positive, and negative charge states, respectively.

To address all these issues, in this paper, we report a more accurate modeling approach for radio frequency (rf) sputter *a*-IGZO TFTs. Section II presents the detailed device structure and mathematical DOS models used in a two-dimensional (2D) numerical simulation. The simulation results are summarized in Sec. III. Finally, the impact of DOS, source/drain (S/D) contact resistances, and OV states on TFT electrical properties are also discussed.

II. 2D NUMERICAL SIMULATION

A 2D inverted-staggered *a*-IGZO TFT structure used for numerical simulation is shown in the inset of Fig. 2(c), and it is designed to match with the actual TFT used in this study (key processing steps are provided in Sec. III A). The structure consists of a 20 nm thick *a*-IGZO active layer and a 100 nm thick thermal SiO₂ gate insulator layer. It should be mentioned that the 2D simulations only calculates the distribution of physical properties along the channel length (L) direction. An ideal, uniform distribution is assumed along the channel width (W) direction. In this study, the TFT (L) and (W) are 30 and 180 μm , respectively. To model the unpassivated *a*-IGZO TFT, the homogeneous Neumann boundary condition²⁰ is applied to the back-channel surface of the *a*-IGZO layer. Such boundary condition prevents carriers from flowing outside of the back-channel surface and ensures that the current only flows in/out of the device through S/D contacts during simulation. Note that both front- and back-channel surfaces of the *a*-IGZO layer are assumed to be ideal, and no interface states are included. The post-thermal annealing step during TFT fabrication is considered to improve the interface quality. This can be further justified by the very low subthreshold swing ($S=0.13$ V/dec) and hysteresis ($\Delta V < 0.2$ V) observed in TFT output properties.

Therefore, the contribution from interface states is thought to be minor in this study. To facilitate the discussion of quantities with different geometrical directions of interest, the X -direction is defined as the channel length direction and the Y -direction is set to be perpendicular to the TFT surface. In addition, since the degenerate conduction might occur in the *a*-IGZO TFT,^{21,22} the Fermi–Dirac statistic is used in numerical simulation.

Contacts between S/D electrodes and the *a*-IGZO layer were either assigned as ohmic or Schottky in nature in this work. In the ohmic contact model, the ideal Dirichlet boundary condition was used,²⁰ and an additional heavily n -type doped (n^+) layer was added at the metal contact/*a*-IGZO interface. For the Schottky model, the S/D metal work function (Ti, $\Phi_m=4.33$ eV) and the electron affinity of *a*-IGZO ($\chi_{a\text{-IGZO}}$) were included in the calculation. Both thermionic emission and tunneling current were considered.²⁰ We estimate $\chi_{a\text{-IGZO}}$ from a simple linear relation between electron affinities of its three elementary compounds (χ with the compound name indicated as a subscript),

$$\chi_{a\text{-IGZO}} = a(\chi_{\text{In}_2\text{O}_3}) + b(\chi_{\text{Ga}_2\text{O}_3}) + c(\chi_{\text{ZnO}}), \quad (1)$$

where a , b , and c are molar percentages (mol %); $\chi_{\text{In}_2\text{O}_3}$, $\chi_{\text{Ga}_2\text{O}_3}$, and χ_{ZnO} are 4.45,²³ 3.19,^{24,25} and 4.5 eV,²⁶ respectively. For *a*-IGZO with an atomic ratio of In:Ga:Zn = 1:1:1 (a , b , and c are 0.25, 0.25, and 0.5, respectively), $\chi_{a\text{-IGZO}}$ was calculated to be 4.16 eV. Throughout this paper, unless otherwise specified, the Schottky contact model is used as a default in numerical simulation.

We set the electron band mobility ($\mu_n=15$ cm²/V s) to be the maximum mobility calculated from TFT transconductance [$\mu_{\text{calc-max}}$, see Eq. (10)]. μ_n is compatible with Hall mobility (μ_{Hall}) extracted from Hall-effect measurements where $\mu_{\text{Hall}}=17$ cm²/V s at a free carrier concentration of 7.8×10^{19} cm⁻³. As a comparison, these mobility values are slightly higher than the Hall mobility (~ 12 cm²/V s) reported for *a*-IGZO deposited by PLD.⁷ The difference is thought to be due to the higher indium composition ratio (x-ray fluorescence measurement showed a composition of In:Ga:Zn=1:1:0.7 in atomic ratio for a film deposited by sputtering with an In:Ga:Zn=1:1:1 target.) and/or the lower trap density of the rf sputter *a*-IGZO thin film. Primarily due to its strong intrinsic n -type nature, by the time this paper is written, p -type conduction of *a*-IGZO has not yet been reported. Most metal oxides have a strong localization behavior of a positive hole at the valence band edge to a single oxygen atom that prevent the hole from freely moving within the crystal lattice.²⁷ As a result, the positive hole constitutes a deep acceptor state, causing a difficulty in achieving p -type conduction and a much lower hole mobility than electron mobility. We believe that a similar situation also exists in *a*-IGZO [Note: Although high mobility p -type conduction has been reported, it only exists in metal oxides with cations that can potentially promote an extended valence band structure (e.g., Cu⁺, Ag⁺, or Au⁺)²⁸]. Therefore, to properly determine the hole mobility (μ_p), we refer to the existing knowledge on ZnO, which is considered to have properties similar to those of *a*-IGZO. In this study, the hole band mobility (μ_p) is chosen to be 0.1 cm²/V s, which is

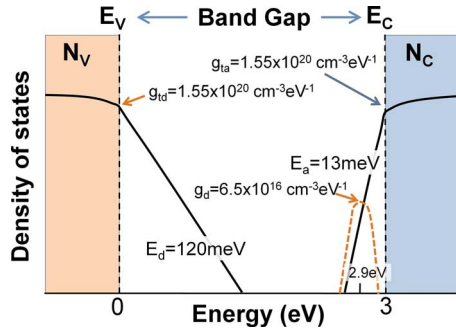


FIG. 1. (Color online) Proposed DOS model for *a*-IGZO. E_C and E_V are conduction and valence band edge energies, respectively. Solid curves within the bandgap represent the exponentially distributed band-tail states (g_{CBa} , g_{VBd}), while the dash curve near the conduction band edge represents the Gaussian-distributed donorlike OV states (g_{Gd}).

close to the values reported for *p*-type ZnO prepared by PLD (0.05–0.4 $\text{cm}^2/\text{V s}$).^{29,30} Higher μ_p values (up to 2 $\text{cm}^2/\text{V s}$) were also tried in simulations, but we observed no appreciable discrepancy in the results (data not shown). This suggests that electron conduction is the dominant mechanism in our *a*-IGZO TFT simulation.

We also developed the DOS model for *a*-IGZO based on several published results. Takagi *et al.*⁷ extracted the conduction band effective mass (m_c) to be $\sim 0.34m_e$ (m_e is the mass of free electron) in their early work on *a*-IGZO. We further calculated the effective conduction band DOS (N_C) to be $5 \times 10^{18} \text{ cm}^{-3}$ at room temperature (300 K) using

$$N_C = 2 \left(\frac{2\pi m_c kT}{h^2} \right)^{3/2}, \quad (2)$$

where $kT = 25 \text{ meV}$ and h is the Planck constant.³¹

The increasing structural disorder within an amorphous material can induce electron scattering and, eventually, localized wave functions. Such phenomenon can be approximately represented as localized tail states within the bandgap, near the band edges.^{15,16} In *a*-IGZO, the conduction band-tail states (g_{CBa}) are thought to originate from the disorder of metal ion *s*-bands, while the oxygen *p*-band disorder mainly contributes to the valence band-tail states (g_{VBd}).³² In this study, the band-tail states of *a*-IGZO are represented as a function of energy (E) by the following expressions (Fig. 1):

$$g_{CBa} = g_{ta} \exp[(E - E_C)/E_a], \quad (3)$$

$$g_{VBd} = g_{td} \exp[(E_V - E)/E_d], \quad (4)$$

where E_C and E_V are conduction and valence band edge energies, g_{ta} and g_{td} are densities of acceptor- and donorlike states at $E = E_C$ and $E = E_V$, respectively, and E_a and E_d are characteristic slopes of conduction and valence band-tail states, respectively. To determine the proper range for g_{ta} , we considered the fact that the DOS has a continuous distribution from tail states to extended states. Therefore, it is reasonable for N_C (or N_V) and g_{ta} (or g_{td}) to have a proportional relation. Since N_C of *a*-IGZO is about an order smaller than *a*-Si:H (N_C for *a*-Si:H is $\sim 3 \times 10^{19} \text{ cm}^{-3}$), we assumed g_{ta} of *a*-IGZO to be around $10^{20} \text{ cm}^{-3} \text{ eV}^{-1}$ (g_{ta} for *a*-Si:H is $10^{21} \text{ cm}^{-3} \text{ eV}^{-1}$).¹⁵ It should be noticed that the range of g_{ta}

and g_{td} determined by this method is consistent with those extracted from x-ray photoelectron spectroscopy experiments.³³ The bandgap (E_g) and valence-band-tail slope (E_d) were further extracted from optical absorption measurements.³⁴ For simplicity, the deep-gap states of *a*-IGZO were not considered in this study. This is justified by a very low deep-gap state concentration of *a*-IGZO (Ref. 3) and a good numerical fit to the experimental data using the proposed DOS model.

OV can also alter the electrical properties of oxide semiconductors. It has been pointed out in the previous section that OV can act like a donor and is double positively charged when fully ionized ($V_O^X \rightarrow V_O^{2+} + 2e'$). Not only could these vacancies exist in the as-deposited film, but as what has been proposed recently, the trace O–H bonds in the *a*-IGZO thin film could react with each other and cause additional OV, such as $M\text{-OH} + M\text{-OH} \rightarrow V_O^{2+} + M\text{-O-M} + \text{H}_2\text{O} \uparrow + 2e'$, where M is the metal cation.³⁵ Although this defect reaction is more complex, the charge state of OV remains the same (+2), and this implies that they can all be modeled as donorlike states.

The energy distribution of OV states is also important. OV states with different degrees of structural relaxation around the vacancy have been simulated by first-principles calculation and have been found to have different energy levels.^{36,37} The local density approximation (LDA) calculation of *a*-IGZO has also shown that the energy level of OV states is located near the conduction band minimum (CBM) for a highly relaxed atomic structure that can be realized by post-thermal annealing or a proper film growth process. On the other hand, if there is no structural relaxation involved, the spatially localized OV state has an energy level closer to the midgap or even valence band minimum (VBM).³⁷ However, since the LDA severely underestimated the bandgap energy, the study is only qualitative, and the exact energy level of the OV state required further study.

The rf sputter *a*-IGZO film used in this work was first deposited on an unheated substrate in the O_2/Ar atmosphere (a total pressure of 0.5 Pa) with an O_2/Ar gas pressure ratio of $\sim 5\%$, followed by a postannealing of 300 °C for 20 min in air. Because our *a*-IGZO has been through a thermal annealing process, we assumed that the near-CBM OV states are dominant in this study, and we used a Gaussian-distributed donorlike state to model the OV in *a*-IGZO,

$$g_{Gd} = g_d \exp[-(E - \lambda)^2/\sigma^2], \quad (5)$$

where g_d , λ , and σ are the peak value, the mean energy, and the standard deviation of states, respectively. The OV states were placed near CBM with $\lambda = 2.9 \text{ eV}$ as a default, but the impact of different energy levels on TFT electrical properties was also investigated. In addition, the energy level of the OV states is assumed to be unchanged after the states are filled with the electrons. It should be noticed that although the numerical simulation can directly assign the doping to *a*-IGZO, it is not possible to simulate the complex carrier trapping behavior of OV states by this approach. To sum up, the schematic of the proposed *a*-IGZO DOS model is illustrated in Fig. 1. During simulation, the DOS equations are modeled with discrete energy levels.²⁰ Even though a large

TABLE I. Key simulation parameters and *a*-IGZO TFT properties.

Symbol	Value	Unit	Description
N_c	5×10^{18}	cm^{-3}	Effective conduction band DOS
N_v	5×10^{18}	cm^{-3}	Effective valence band DOS
g_{ta}	1.55×10^{20}	$\text{cm}^{-3} \text{eV}^{-1}$	Density of tail states at $E=E_C$
g_{td}	1.55×10^{20}	$\text{cm}^{-3} \text{eV}^{-1}$	Density of tail states at $E=E_V$
E_a	13	meV	Conduction-band-tail slope
E_d	120	meV	Valence-band-tail slope
E_g	3.05	eV	Bandgap
χ	4.16	eV	Electronic affinity
ϵ	10		Permittivity
μ_n	15	$\text{cm}^2/\text{V s}$	Band mobility (electron)
μ_p	0.1	$\text{cm}^2/\text{V s}$	Band mobility (hole)
m_c	0.34	m_e	Conduction band effective mass
g_d	6.5×10^{16}	$\text{cm}^{-3} \text{eV}^{-1}$	Peak of OV states
λ	2.9	eV	Mean energy of OV states
σ	0.1	eV	Standard deviation of OV states
<i>a</i> -IGZO TFT properties			
μ_{eff}	12	$\text{cm}^2/\text{V s}$	Field-effect mobility
V_{th}	1.15	V	Threshold voltage
S	0.13	V/dec	Subthreshold swing
I_{off}	$<10^{-14}$	A	Off current
	10^{10}		On/off current ratio

number of energy levels can promise a better accuracy, it can also increase the calculation time significantly. In this work, we optimized the setting to 128 and 64 levels for acceptor- and donorlike states, respectively (or Acc./Don.=128/64 levels). Compared to this optimized setting, simulation with larger number of energy levels (e.g. Acc./Don.=1000/500 levels) show a marginal difference in drain current (~ 40 nA) which only occurs in TFT on-region.

III. RESULTS AND DISCUSSION

A. Electrical properties of the *a*-IGZO TFT

The experimental data were measured for the *a*-IGZO TFT with a common gate, inverted-staggered structure.¹² A heavily P-doped (n^{++}) silicon wafer and a 100 nm thermal SiO₂ layer was used as a gate electrode and a gate insulator, respectively. A 20 nm thick *a*-IGZO active layer was deposited on the unheated substrate by rf magnetron sputtering from a polycrystalline InGaZnO₄ target. The film was deposited in the mixtures of Ar and O₂ gases under a total pressure of 0.5 Pa with an O₂ partial pressure of 25 mPa. *a*-IGZO was patterned by a diluted HCl wet-etching process and was then thermally annealed at 300 °C for 20 min in air. Finally, the Au/Ti stacked layer (40/5 nm thick) was deposited as S/D electrodes and was patterned by a lift-off technique. It should be noticed that there is no passivation layer in the device used in this work.

All the parameters extracted from experimental data used in this numerical simulation are listed in Table I. The listed threshold voltage (V_{th}) and field-effect mobility (μ_{eff}) were extracted based on the standard metal-oxide-semiconductor field-effect transistor (MOSFET) equation,¹⁵

$$I_D = \mu_{\text{eff}} C_{\text{ox}} \frac{W}{L} (V_{GS} - V_{\text{th}}) V_{DS}, \quad (6)$$

where I_D is the drain current, V_{GS} is the gate bias voltage, V_{DS} is the drain bias voltage, C_{ox} is the gate insulator capacitance per unit area, and W and L are the TFT channel width and length, respectively. V_{th} and μ_{eff} were extracted from the best linear fit of Eq. (6) to I_D versus V_{GS} characteristics between 90% and 10% of the maximum I_D (at $V_{GS}=20$ V). In addition, a nonlinearity of I_D versus V_{GS} , which is associated with g_{CBA} , was observed and will be discussed in Sec. III B. The subthreshold swing (S) was also extracted from the subthreshold region data at the maximum slope point [Fig. 2(c)] using¹⁵

$$S = \left(\frac{\delta \log(I_D)}{\delta V_{GS}} \right)^{-1}. \quad (7)$$

Very highly accurate output (rms error $< 8 \mu\text{A}$), transfer (< 26 nA), and subthreshold (< 17 nA) *a*-IGZO TFT experimental characteristics were reproduced by our model (Fig. 2). Simulation results based on the S/D ohmic contact models are also shown in Fig. 2. The ohmic contact model only gives a slightly higher drain current (for example, less than 1% increase under linear region) in comparison to the Schottky (Ti) contact model. This suggests that the Schottky barrier height ($\Phi_n = \Phi_m - \chi = 0.17$ eV) for the Ti S/D metal is small, and Ti forms an ohmic-like contact with the *a*-IGZO layer.

To better understand the *a*-IGZO TFT operation, the cross sectional view of the simulated drain current flow (vector plot) near the drain electrode, when the *a*-IGZO TFT is operated under a linear region ($V_{DS}=0.1$ V, $V_{GS}=20$ V), is illustrated in Fig. 3. The free electron concentration (n) is also shown as a contour plot. The results reveal a high concentration of free electrons ($n > 10^{19} \text{cm}^{-3}$) accumulated near the gate insulator/*a*-IGZO interface; this “channel layer” carries the majority of the drain current. In addition, the channel current flow extends to about $0.7 \mu\text{m}$ below the drain electrode, which is approximately similar to the transfer length ($\sim 0.5 \mu\text{m}$) extracted from the transmission line analysis (TLM).³⁸ The dependences of n and current density (J) on V_{GS} were also studied. Figures 4(a) and 4(b) show a simulated distribution of n and the X -component of the current density (J_X) at the center of the *a*-IGZO TFT structure. When the TFT is operated in the on region ($V_{GS} > V_{\text{th}}$), a non-negligible number of electrons accumulate near the back channel ($n \sim 10^{17} \text{cm}^{-3}$) that corresponds to about $0.1 \mu\text{A}/(\mu\text{m})^2$ of drain current. Hence, the back-channel current can contribute a major portion of the total channel current under a low V_{GS} condition. Therefore, it is important/critical to passivate the back channel in *a*-IGZO TFTs. It should be noticed that the Y -component of the current density (J_Y) is essentially zero compared to J_X . Therefore, the current flows uniformly along the channel length direction at the center of the device. In fact, the 20 nm thick *a*-IGZO layer is very thin, so the Fermi level (E_F) of the entire film moves toward the conduction band (E_C) in the subthreshold

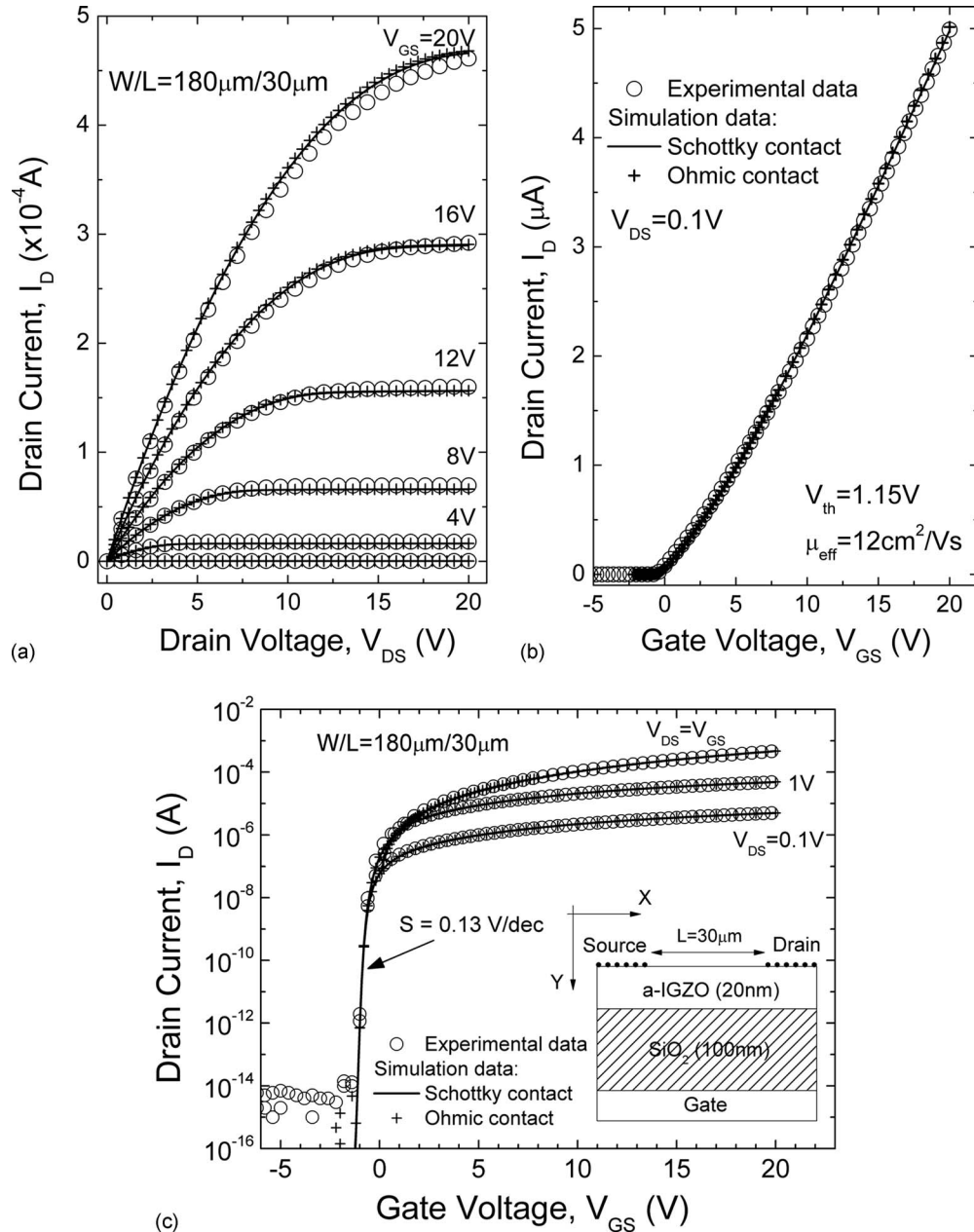


FIG. 2. *a*-IGZO TFT: (a) output and [(b) and (c)] transfer characteristics ($W/L=180/30 \mu\text{m}$). Both experimental (\circ) and simulation data (solid line: Schottky contact; +: Ohmic contact) are shown. Extracted threshold voltage (V_{th}), field-effect mobility (μ_{eff}), and subthreshold swing (S) are also indicated. Inset of (c): the 2D TFT structure used in simulation. This structure is further decomposed into smaller mesh structures for a finite element analysis.

region [Fig. 4(c)]. Hence, the conventional assumption of the back channel as a “bulk,” with the E_F position being the same as it is under thermal equilibrium, is not valid here. In the on region, the E_F of the back channel is approximately pinned at 0.1 eV below E_C , and the band bending starts to occur near the *a*-IGZO/SiO₂ interface (front channel) as V_{GS} increased. The degree of band bending increases with V_{GS} , and E_F can move into E_C under a high V_{GS} condition (i.e., $E_C - E_F < 0$ V at $V_{GS} = 20$ V). This suggests that a high electron concentration channel layer in *a*-IGZO, illustrated in Fig. 3, is in its degenerate state, which is an important factor to achieve a high-performance TFT. Our simulation results also provide the physical insight of the sensitive dependence of the *a*-IGZO TFT I/V properties on back-channel conditions reported by other groups.^{39,40}

B. The impact of conduction band-tail slope (E_a) and S/D contact resistance (r_c)

Impacts of the DOS properties and S/D contact resistance (r_c) on TFT performance were also investigated. Based on the default model (parameters are listed in Table I), the conduction band-tail slope (E_a) was changed from 13 to 35 meV. The simulated linear region I/V data ($V_{DS}=0.1$ V) for various E_a values are shown in Fig. 5. The simulation indicates that a higher E_a could induce a significant decrease in TFT drain current. To clarify its physical origin, the band bending near the *a*-IGZO/SiO₂ interface for different E_a was first investigated. The Fermi-level position relative to the conduction band edge ($E_C - E_F$) is plotted as a function of V_{GS} [Fig. 6(a)]. Clearly, the movement of E_F toward E_C is

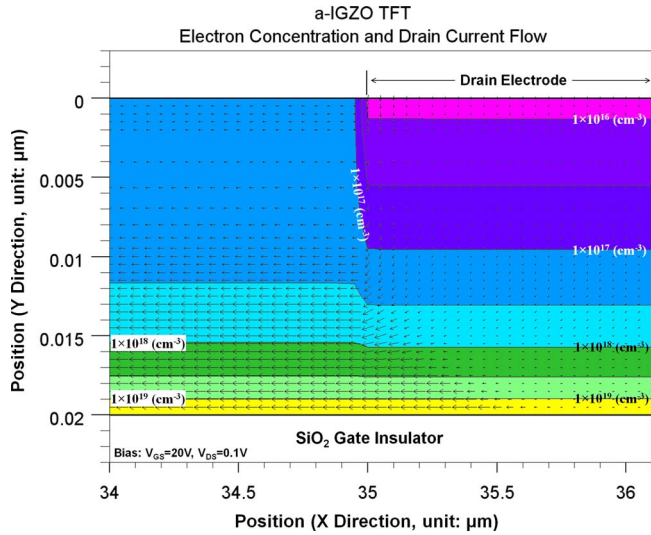


FIG. 3. (Color online) A zoom-in view of the simulated TFT structure near the drain electrode. The contour distribution of the free electron concentration within the *a*-IGZO layer is shown. The X-direction is parallel to the TFT channel length direction, while the Y-direction is perpendicular to the device surface. The arrow represents the vector for current density at each mesh grid point, and the length of the arrow is proportional to the magnitude of the current density. (Bias condition: $V_{GS}=20$ V and $V_{DS}=0.1$ V.)

smaller for TFT with a higher E_a , and it will take a higher V_{GS} to reach the same amount of E_C-E_F . Such effect is directly related to the increase in g_{CBa} . As a result, the maximum achievable band bending decreases, which lowers the free electron concentration in the conducting channel and reduces the drain current.

Besides the reduction in I_D , the observed nonlinearity of I_D-V_{GS} was also investigated. It is proposed that to describe the nonlinear *a*-IGZO TFT I/V behavior, the gate voltage dependent field-effect mobility [$\mu_{\text{eff}}(V_{GS})$] should be adopted,⁴¹

$$\mu_{\text{eff}}(V_{GS}) = K(V_{GS} - V_{\text{th}})^\alpha. \quad (8)$$

In the above equation, α is the exponent to account for voltage dependence and K is a material dependent constant. It is believed that for the *a*-IGZO TFT, a portion of the total induced channel charges (electrons) are trapped in band-tail states and cannot contribute to I_D . As V_{GS} increased, more free electrons are able to contribute to I_D , and this makes μ_{eff} to increase with V_{GS} with a nonideal exponent of $\alpha > 0$ (or $\gamma > 1$). By introducing Eq. (8) into Eq. (6), the nonlinear drain current equation can be derived,

$$I_D = KC_{\text{ox}} \frac{W}{L} (V_{GS} - V_{\text{th}})^\gamma V_{DS}, \quad (9)$$

where $\gamma \equiv \alpha + 1$. As a comparison, in the ideal case (i.e., where there is no band-tail state and all the induced electrons are able to participate in drain current conduction), $\alpha = 0$ (or $\gamma = 1$) and μ_{eff} (or K) is equal to the electron band mobility (μ_n). The gamma factor (γ) can be extracted from the field-effect mobility calculated from TFT transconductance (μ_{calc}) using the following mathematical relation:⁴²

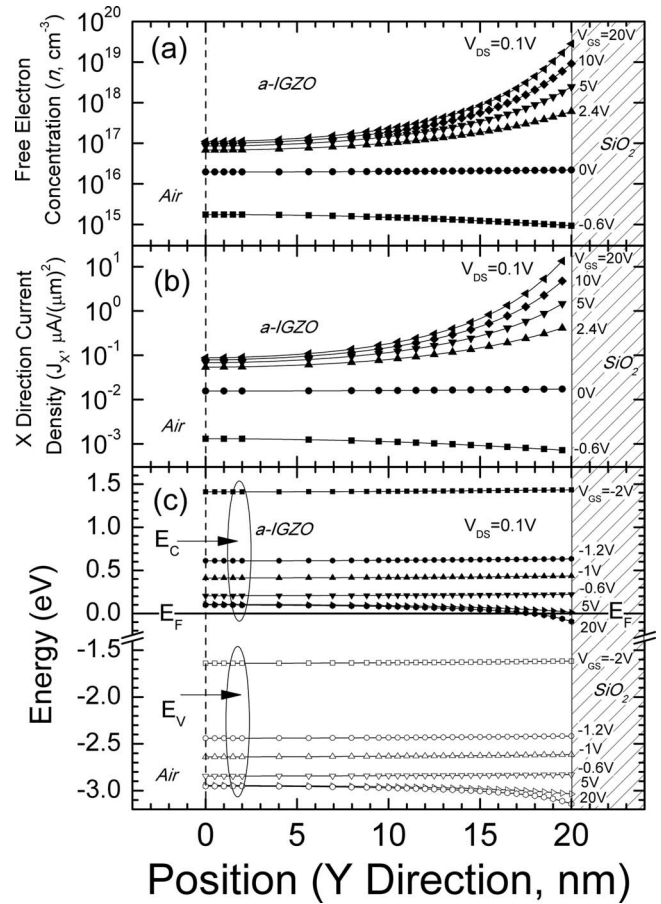


FIG. 4. Simulated distribution of (a) the free electron density (n) and (b) the X-direction current density (J_X) at the center of the *a*-IGZO TFT structure. The gate voltage was changed from -0.6 up to 20 V. The film thickness of *a*-IGZO is 20 nm. Position $Y=0$ represents the back-channel surface, while $Y=20$ nm represents the interface between *a*-IGZO and the SiO_2 gate insulator. (c) Simulated energy band bending diagram at the center of the *a*-IGZO TFT structure. The electron quasi-Fermi level (E_F) was used as a reference energy level for all simulation results (energy=0 eV). The gate voltage was changed from -2 up to 20 V. Closed symbols: conduction band edge energy (E_C); open symbols: valence band edge energy (E_V).

$$\mu_{\text{calc}} = \left(\frac{\delta I_D}{\delta V_{GS}} \right) \frac{L}{WC_{\text{ox}} V_{DS}} = K\gamma(V_{GS} - V_{\text{th}})^{\gamma-1}. \quad (10)$$

It should be noticed that under a small V_{DS} assumption ($V_{DS} \ll V_{GS} - V_{\text{th}}$), μ_{calc} is approximately equal to the incremental mobility (μ_{inc}) proposed by Hoffman in his earlier

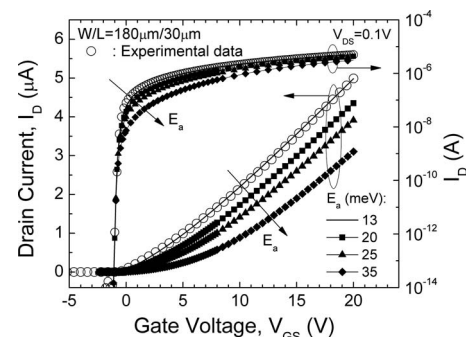


FIG. 5. Simulated *a*-IGZO TFT linear region transfer curves for both linear and semilogarithm scales for various E_a values are shown. The experimental data (symbol: \circ) are also shown.

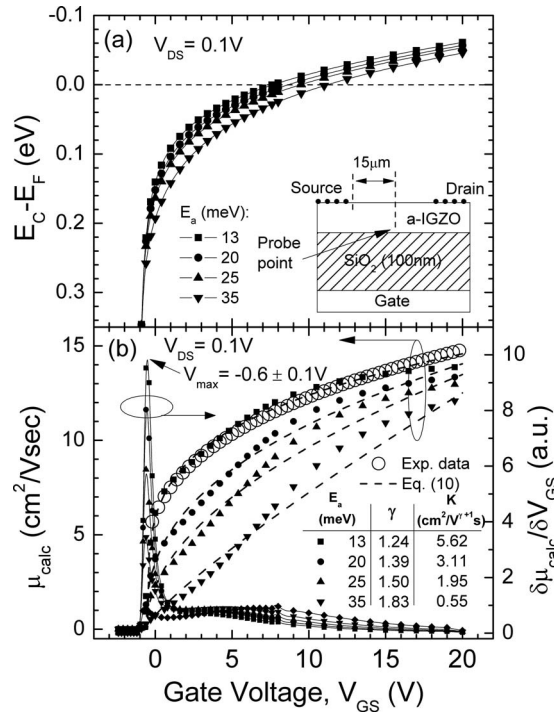


FIG. 6. (a) Simulated *a*-IGZO Fermi-level position vs gate voltage (V_{GS}). The Fermi-level position is represented as $E_C - E_F$, where E_C and E_F are the energies for the conduction band edge and the Fermi level, respectively. The inset indicates the probe point for this data, and it is located at the center of the TFT, near (0.5 nm away from) the *a*-IGZO/SiO₂ interface. The slight offset is to avoid the calculation discontinuity that might occur at the interface. (b) The μ_{calc} and $\delta\mu_{\text{calc}}/\delta V_{GS}$ extracted from simulated *a*-IGZO TFT transfer characteristics for various E_a values. The experimental data (symbol: \circ) are also shown. Dash lines are the model fitting curves based on Eq. (10), and the parameters used in the model are illustrated in the inset.

work.⁴³ We followed a two step process for parameter extraction, which is described elsewhere:⁴¹ the V_{th} is first determined as the V_{GS} value at which maximum $\delta\mu_{\text{calc}}/\delta V_{GS}$ occurs (i.e., $V_{\text{th}} = V_{\text{max}}$); then, K and γ are extracted from the best linear fit of the $\log(\mu_{\text{calc}})$ versus $\log(V_{GS} - V_{\text{th}})$ plot based on Eq. (10) (data not shown). As illustrated in Fig. 6(b), the field-effect mobility is actually a function of V_{GS} . It increases with V_{GS} and, for the case of $E_a = 13$ meV, approaches the band mobility ($15 \text{ cm}^2/\text{V s}$) when $V_{GS} = 20$ V. The dependence of μ_{calc} on E_a is also included in Fig. 6(b), and a significant decrease in μ_{calc} is observed for higher E_a . Although the simple power law dependence [Eq. (8)] is not able to accurately model the complex V_{GS} dependence of μ_{calc} for higher E_a (i.e., 35 meV), it still shows that the higher γ -values (e.g., $\gamma = 1.83$ when $E_a = 35$ meV) are obtained as compared to the one extracted for lower E_a (e.g., $\gamma = 1.24$ when $E_a = 13$ meV). This suggests that the degree of nonlinearity increases with E_a , and consequently, the field-effect mobility has a stronger dependence on V_{GS} . In addition, V_{th} (or V_{max}) is fairly constant (~ -0.6 V) for all E_a values (13–35 meV). This gate voltage (-0.6 V) correlates to $E_C - E_F$ of 0.22–0.26 eV, where the $E_C - E_F$ versus V_{GS} starts to have a strong dependence on E_a [Fig. 6(a)]. (In Fig. 7, the corresponding total ionized acceptorlike states (n_{acceptor}^-) range from 10^{15} to 10^{16} cm^{-3} .) Therefore, in this simulation the V_{max} is able to consistently be associated with the V_{th} point at which E_F reaches the raising edge of conduc-

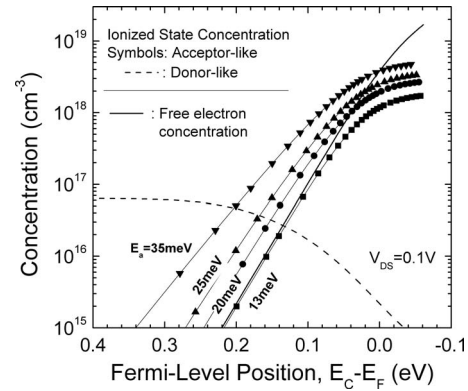


FIG. 7. Simulated free electron concentration (n), ionized acceptorlike states (n_{acceptor}^-), and ionized donorlike states (n_{donor}^+) as a function of $E_C - E_F$. All the concentration data are integrated values over all energy levels within the bandgap. The symbols represent n_{acceptor}^- for various E_a values, while the solid and dash lines are n and n_{donor}^+ , respectively. Since the data for n and n_{donor}^+ are the same for different E_a , only one data line is shown. The probe point is the same as indicated in the inset of Fig. 6(a).

tion band-tail states in spite of the increasing nonlinearity in I - V characteristics. This condition cannot be observed when V_{th} is extracted from the ideal MOSFET model [Eq. (6)]. For example, the V_{th} extracted from Eq. (6) significantly shifts from 1.15 V (for $E_a = 13$ meV) to 4.79 V when $E_a = 35$ meV.

Figure 7 analyzes the concentration of free electrons (n), ionized donorlike states (n_{donor}^+), and ionized acceptorlike states (n_{acceptor}^-) and plots them as a function of the Fermi-level position ($E_C - E_F$). To avoid confusion, it should be recalled that E_a can affect the gate voltage dependence of $E_C - E_F$ [Fig. 6(a)], and one should not expect the same $E_C - E_F$ value to be achieved under the same V_{GS} for different cases. It should also be noticed that n_{donor}^+ is primarily contributed by the ionized OV states: when $E_C - E_F > 0.3$ eV, all the OV states are ionized but start to be filled/passivated by electrons when $E_C - E_F < 0.3$ eV. Since n_{donor}^+ is one to two orders of magnitudes lower than n and n_{acceptor}^- in most $E_C - E_F$ ranges of interest, we only focus on n and n_{acceptor}^- in the following discussion. Our default model has an E_a of 13 meV. Such sharp distribution of conduction band-tail states (g_{CBa}) allows for n to be the dominant contribution to the total gate induced carriers. For instance, when $V_{GS} = 20$ V, $E_C - E_F \sim -0.06$ eV and the ratio n/n_{acceptor}^- can be as high as ~ 10 . Also, as expected, $E_a = 13$ meV is lower than the common *a*-Si:H value (~ 25 meV) and agrees fairly well with the prediction of Kamiya *et al.*⁴⁴ in their original work. However, for the TFT with a higher E_a (20–35 meV), most of the accumulated electrons are trapped by the conduction band-tail states. This trapping process decreases the ratio of n/n_{acceptor}^- (< 1 for most of the $E_C - E_F$ values), and it will take a larger surface band bending (i.e., $E_C - E_F < 0.05$ eV) and V_{GS} for this ratio to be larger than unity. The phenomenon caused by this effect is twofold: First, since the concentration of n is lower, the maximum achievable μ_{calc} decreases. Second, an increasing degree of nonlinearity in drain current (i.e., γ) is expected as experimentally observed.

With the default Schottky contact model, r_c values varied from 0–0.27 $\Omega \text{ cm}^2$ in a logarithmic increment. A per-

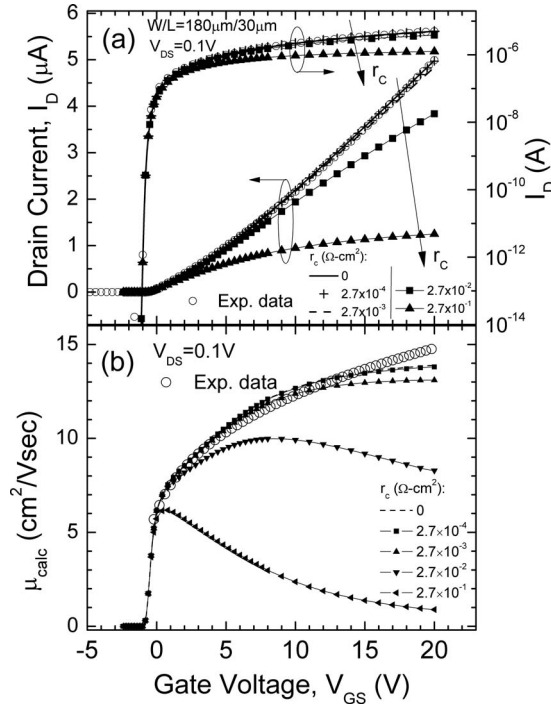


FIG. 8. Simulated *a*-IGZO TFT: (a) linear region transfer curves and (b) μ_{calc} extracted from TFT transfer characteristics for various r_c values. The experimental data (symbol: \circ) are also shown.

ceivable decrease in the simulated *a*-IGZO TFT linear region drain current ($>3\%$) only exists when $r_c > 2.7 \times 10^{-3} \Omega \text{ cm}^2$ [Fig. 8(a)]. This implies that r_c for the actual TFT could be in the $\sim 10^{-4} \Omega \text{ cm}^2$ range. This is consistent with the result obtained from the TLM analysis,³⁸ suggesting that the contact resistance can be as low as $\sim 4 \times 10^{-4} \Omega \text{ cm}^2$. In practice, a feature that can be used to differentiate between g_{CBa} and r_c induced I_D reduction could be very helpful. This task would be more easily accomplished by inspecting the μ_{calc} versus V_{GS} plots [Fig. 8(b)]. μ_{calc} for TFT with excess r_c decreases at high V_{GS} ; such effect yields a unique “maximum” hump in the μ_{calc} versus V_{GS} plot. This is thought to be due to the increasing voltage drop at the S/D contact at higher I_D , which adversely lowers the effective voltage drop across the source to drain channel. The existence of the μ_{calc} maximum is a unique feature for TFT having larger r_c (but not for TFT having high E_a) and might be used for diagnostic purposes of the TFT S/D contact quality.

C. The impact of OV states

Figure 9 shows the simulation result for different OV state peak values (g_d) ranging from 6.5×10^{16} to $5 \times 10^{17} \text{ cm}^{-3} \text{ eV}^{-1}$. We found that an increasing g_d can cause a negative shift in TFT transfer characteristic, and this trend agreed very well with what have been reported for PLD *a*-IGZO TFT.¹³ Accompanied with a negative shift, both the subthreshold swing (S) and the TFT off current increase [Fig. 9(b)]. In other words, *a*-IGZO loses its semiconducting property and behaves more like a conductor with increasing g_d . The simulation also suggests such effect to be very sensitive to the g_d value; e.g., an approximately eight times increase in g_d can cause a reduction in on/off ratio by more than seven

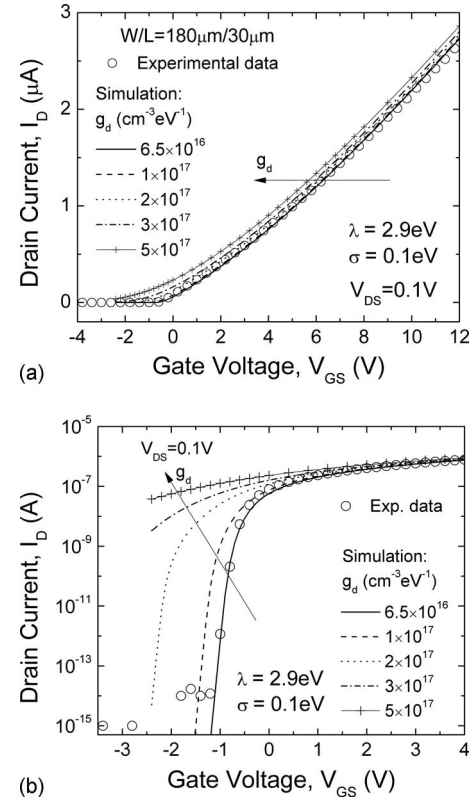


FIG. 9. *a*-IGZO TFT simulated linear region I_D - V_{GS} curves in (a) the linear scale and (b) the semilogarithmic scale for various OV state peak values (g_d). Real experimental data (\circ) are also shown as reference.

orders of magnitude. Figure 10 illustrates the n_{donor}^+ and V_{GS} as a function of $E_C - E_F$. Per discussion in the previous section, n_{donor}^+ is thought to be primarily associated with the ionized OV states (g_{Gd}). For the default condition ($g_d = 6.5 \times 10^{16} \text{ cm}^{-3} \text{ eV}^{-1}$), all the g_{Gd} states are ionized in the subthreshold and off regions (i.e., n_{donor}^+ is a constant $\sim 6 \times 10^{16} \text{ cm}^{-3}$ for $E_C - E_F > 0.3 \text{ eV}$). When g_d increases, the positive charged n_{donor}^+ also increases, and to maintain the charge neutrality within *a*-IGZO, E_F needs to move closer to E_C to induce a larger density of electrons. For example, for $V_{\text{GS}} = -1.5 \text{ V}$, the $E_C - E_F$ moves from 0.93 eV ($g_d = 6.5 \times 10^{16} \text{ cm}^{-3} \text{ eV}^{-1}$) to 0.16 eV when $g_d = 5 \times 10^{17} \text{ cm}^{-3} \text{ eV}^{-1}$. In fact, the g_{Gd} states are only partially

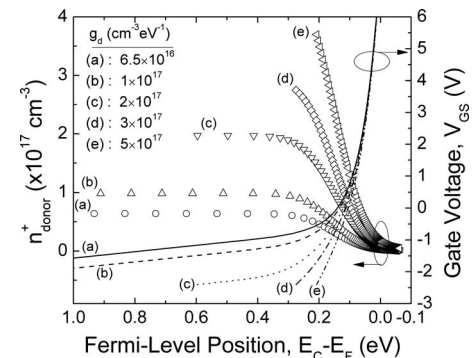


FIG. 10. Simulated ionized donorlike state concentration (n_{donor}^+) and gate voltage (V_{GS}) as a function of the Fermi-level position ($E_C - E_F$) for various OV state peak values (g_d). The probe point is the same as indicated in the inset of Fig. 6(a).

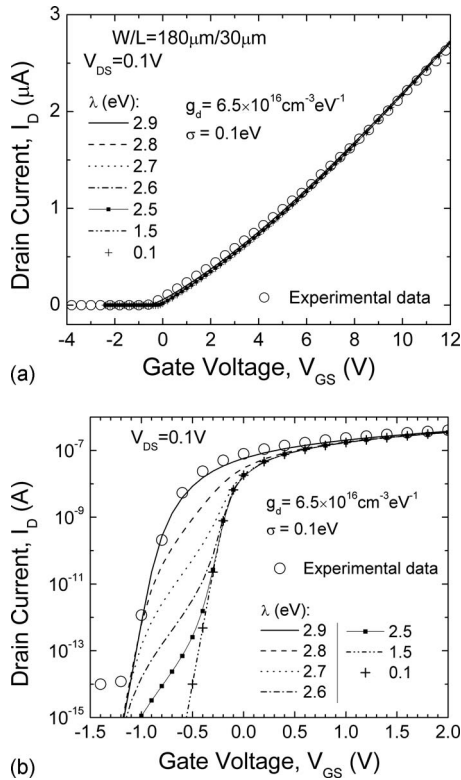


FIG. 11. *a*-IGZO TFT simulated linear region I_D - V_{GS} curves in (a) the linear scale and (b) the semilogarithmic scale for various OV state mean energies (λ). Real experimental data (\circ) are also shown as reference.

ionized for $g_d > 3 \times 10^{17} \text{ cm}^{-3} \text{ eV}^{-1}$; this is because the Fermi level is located within the energy range of g_{Gd} states for these conditions. The above mentioned mechanism is similar to doping despite the lack of involvement of actual dopants. Furthermore, the author of this paper believed that such effect is consistent with the “intrinsic doping” concept proposed by other groups.^{9,11,45}

Since the mean energy (λ) of OV states within the bandgap can change if structural relaxation occurs,³⁶ such effect was also investigated. Figure 11 illustrates the effect of g_{Gd} states located at seven different energy levels within the bandgap ($\lambda = 2.9, 2.8, 2.7, 2.6, 2.5, 1.5,$ and 0.1 eV). Although the impact on on-region TFT I/V properties is minimum [In Fig. 11(a), it is thought to be due to a lower g_{Gd} concentration compared to the g_{CBa} concentration], the subthreshold properties do depend on λ [Fig. 11(b)]. By changing λ from 2.9 to 1.5 eV, there is about +0.6 V of shift in transfer characteristics. In addition, an increase (or, more accurately, a “distortion”) in the subthreshold swing/region was observed during the transition phase. From the previous simulation, we know that the Fermi level approximately moves from 0.9 eV below E_C toward E_C during the TFT operation. Before the E_F overlaps with the energy range of g_{Gd} states, they are all fully ionized, and when E_F moves across the g_{Gd} states ($E_C - E_F < 0.3 \text{ eV}$), these states start to be filled by electrons, and therefore, n_{donor}^+ decreases. In the default model, the decrease in n_{donor}^+ primarily occurs in the on region (Figs. 10 and 12). However, the situation changes when λ is located closer to the midgap. As shown in Fig. 12, the decrease in n_{donor}^+ occurs at a much higher value of $E_C - E_F$ (0.4–0.7 eV)

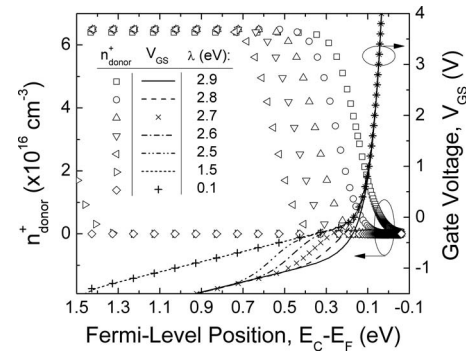


FIG. 12. Simulated ionized donorlike state concentration (n_{donor}^+) and gate voltage (V_{GS}) as a function of the Fermi-level position ($E_C - E_F$) for various OV state mean energies (λ). The probe point is the same as indicated in the inset of Fig. 6(a).

for $\lambda = 2.8$ – 2.5 eV . This range overlaps with the subthreshold region and causes the observed degradation in simulated subthreshold swing properties. When λ is located at the mid-gap (1.5 eV) or even closer to VBM (0.1 eV), the g_{Gd} states are well below the initial Fermi-level position. As a result, instead of fully ionized, g_{Gd} states with $\lambda < 1.5 \text{ eV}$ are mostly or fully filled/passivated by electrons (i.e., $n_{\text{donor}}^+ \ll 10^{16} \text{ cm}^{-3}$, Fig. 12). This allows the Fermi level to move closer toward the midgap and induces the positive shift observed in the transfer characteristics. In addition, since E_F is not within the energy range of g_{Gd} states, the subthreshold swing is not affected. It should be noticed that g_{Gd} represents the electronically effective density, and the actual OV density (D_{OV}) should be written as $D_{OV} = g_{Gd} / Z_{OV}$, where Z_{OV} is the charge state of OV. For instance, as suggested by the first-principles calculation, Z_{OV} are +2 and +1 when the OV states are near CBM and midgap, respectively.³⁶ Finally, our observations also agree well with the conclusions drawn from the first-principles calculation on *a*-IGZO,³⁷ which suggests that the energy locations of OV states should be properly controlled (i.e., through processing) to achieve a high-performance *a*-IGZO TFT.

IV. CONCLUSION

We have developed the *a*-IGZO DOS model that is suitable for a 2D numerical simulation of the rf sputter *a*-IGZO TFT. Experimental TFT electrical properties were precisely reproduced by numerical simulation, and the results suggest that our rf sputter *a*-IGZO TFT has a nonrectifying S/D contact with low r_c ($< 2.7 \times 10^{-3} \Omega \text{ cm}^2$) and a sharp conduction band-tail slope ($E_a = 13 \text{ meV}$). The model can also predict the change in TFT electrical properties for different OV state conditions. The reported 2D numerical simulation technique can be a useful tool for engineers to understand the device operation and optimize *a*-IGZO TFT electrical performance.

ACKNOWLEDGMENTS

The authors at the University of Michigan (T.-C.F., C.C., and J.K.) would like to gratefully acknowledge the support

from Canon Research Center, Canon, Inc., DARPA/MTO HARDI program (Dr. Devanand K. Shenoy), and AKT America, Inc.

- ¹J.-H. Lee, D.-H. Kim, D.-J. Yang, S.-Y. Hong, K.-S. Yoon, P.-S. Hong, C.-O. Jeong, H.-S. Park, S. Y. Kim, S. K. Lim, S. S. Kim, K.-S. Son, T.-S. Kim, J.-Y. Kwon, and S.-Y. Lee, *SID Int. Symp. Digest Tech. Papers* **2008**, 625.
- ²J. K. Jeong, J. H. Jeong, J. H. Choi, J. S. Im, S. H. Kim, H. W. Yang, K. N. Kang, K. S. Kim, T. K. Ahn, H.-J. Chung, M. Kim, B. S. Gu, J.-S. Park, Y.-G. Mo, H. D. Kim, and H. K. Chung, *SID Int. Symp. Digest Tech. Papers* **2008**, 1.
- ³T.-C. Fung, C.-S. Chuang, K. Nomura, H.-P. D. Shieh, H. Hosono, and J. Kanicki, *Information Display (J. Korean Information Display Society)* **9**, 21 (2008).
- ⁴T.-C. Fung, C.-S. Chuang, B. G. Mullins, K. Nomura, T. Kamiya, H.-P. D. Shieh, H. Hosono, and J. Kanicki, *Digest of Technical Papers of International Meeting on Information Display (IMID)*, 2008, Vol. 8, p. 1208.
- ⁵K. Nomura, H. Ohta, A. Takagi, T. Kamiya, M. Hirano, and H. Hosono, *Nature (London)* **432**, 488 (2004).
- ⁶H. Hosono, *J. Non-Cryst. Solids* **352**, 851 (2006).
- ⁷A. Takagi, K. Nomura, H. Ohta, H. Yanagi, T. Kamiya, M. Hirano, and H. Hosono, *Thin Solid Films* **486**, 38 (2005).
- ⁸H. Hosono, M. Yasukawa, and H. Kawazoe, *J. Non-Cryst. Solids* **203**, 334 (1996).
- ⁹K. Nomura, A. Takagi, T. Kamiya, H. Ohta, M. Hirano, and H. Hosono, *Jpn. J. Appl. Phys., Part 1* **45**, 4303 (2006).
- ¹⁰A. Suresh, P. Wellenius, A. Dhawan, and J. Muth, *Appl. Phys. Lett.* **90**, 123512 (2007).
- ¹¹H. Kumomi, K. Nomura, T. Kamiya, and H. Hosono, *Thin Solid Films* **516**, 1516 (2008).
- ¹²R. Hayashi, M. Ofuji, N. Kaji, K. Takahashi, K. Abe, H. Yabuta, M. Sano, H. Kumomi, K. Nomura, T. Kamiya, M. Hirano, and H. Hosono, *J. SID* **15**, 915 (2007).
- ¹³H.-H. Hsieh, T. Kamiya, K. Nomura, H. Hosono, and C.-C. Wu, *Appl. Phys. Lett.* **92**, 133503 (2008).
- ¹⁴K. Jeon, C. Kim, I. Song, J. Park, S. Kim, S. Kim, Y. Park, J.-H. Park, S. Lee, D. M. Kim, and D. H. Kim, *Appl. Phys. Lett.* **93**, 182102 (2008).
- ¹⁵J. Kanicki and S. Martin, in *Thin-Film Transistors*, edited by C. R. Kagan and P. Andry (Dekker, New York, 2003), pp. 71–137.
- ¹⁶R. A. Street, *Hydrogenated Amorphous Silicon* (Cambridge University Press, Cambridge, England, 1991).
- ¹⁷M. Shur and M. Hack, *J. Appl. Phys.* **55**, 3831 (1984).
- ¹⁸C.-Y. Chen and J. Kanicki, *Proceedings of the International Workshop on Active Matrix Liquid Crystal Displays (AMLCD'95)*, 1995, pp. 46–49.
- ¹⁹P. Kofstad, *Nonstoichiometry, Diffusion, and Electrical Conductivity in Binary Metal Oxides* (Wiley Interscience, New York, 1972).
- ²⁰*ATLAS Device Simulation Software User's Manual* (Silvaco, Santa Clara, CA, 2005).
- ²¹H. Hosono, N. Kikuchi, N. Ueda, and H. Kawazoe, *J. Non-Cryst. Solids* **198–200**, 165 (1996).
- ²²M. Orita, H. Ohta, M. Hirano, S. Narushima, and H. Hosono, *Philos. Mag. B* **81**, 501 (2001).
- ²³L. Hsu and E. Y. Wang, *13th IEEE Photovoltaic Specialists Conference* (IEEE, New York, 1978), pp. 536–540.
- ²⁴E. F. Archibong and E. N. Mvula, *Chem. Phys. Lett.* **408**, 371 (2005).
- ²⁵S. Gowtham, M. Deshpande, A. Costales, and R. Pandey, *J. Phys. Chem. B* **109**, 14836 (2005).
- ²⁶K. Jacobi, G. Zwicker, and A. Gutmann, *Surf. Sci.* **141**, 109 (1984).
- ²⁷H. Kawazoe, H. Yanagi, K. Ueda, and H. Hosono, *MRS Bull.* **25**, 28 (2000).
- ²⁸H. Kawazoe, M. Yasukawa, H. Hyodo, M. Kurita, H. Yanagi, and H. Hosono, *Nature (London)* **389**, 939 (1997).
- ²⁹X.-L. Guo, H. Tabata, and T. Kawai, *J. Cryst. Growth* **223**, 135 (2001).
- ³⁰M. Joseph, H. Tabata, H. Saeki, K. Ueda, and T. Kawai, *Physica B* **302–303**, 140 (2001).
- ³¹R. S. Muller, T. I. Kamins, and M. Chan, *Device Electronics for Integrated Circuits*, 3rd ed. (Wiley, New York, 2003).
- ³²J. Robertson, *J. Non-Cryst. Solids* **354**, 2791 (2008).
- ³³K. Nomura, T. Kamiya, H. Yanagi, E. Ikenaga, Y. Ke, K. Kobayashi, M. Hirano, and H. Hosono, *Appl. Phys. Lett.* **92**, 202117 (2008).
- ³⁴C.-S. Chuang, T.-C. Fung, B. G. Mullins, K. Nomura, T. Kamiya, H.-P. D. Shieh, H. Hosono, and J. Kanicki, *SID Int. Symp. Digest Tech. Papers* **2008**, 1215.
- ³⁵K. Nomura, T. Kamiya, H. Ohta, M. Hirano, and H. Hosono, *Appl. Phys. Lett.* **93**, 192107 (2008).
- ³⁶A. Janotti and C. G. Van De Walle, *Appl. Phys. Lett.* **87**, 122102 (2005).
- ³⁷T. Kamiya, K. Nomura, M. Hirano, and H. Hosono, *Phys. Status Solidi C* **5**, 3098 (2008).
- ³⁸The TLM analysis was conducted using the method outlined in Ref. 15, with TFT L ranging from 10~60 μm and V_{GS} ranging from 10~20 V.
- ³⁹K. Donghun, L. Hyuck, K. Changjung, S. Ihun, J. Park, P. Youngsoo, and C. JaeGwan, *Appl. Phys. Lett.* **90**, 192101 (2007).
- ⁴⁰J. Jae Kyeong, Y. Hui Won, J. Jong Han, M. Yeon-Gon, and K. Hye Dong, *Appl. Phys. Lett.* **93**, 123508 (2008).
- ⁴¹T.-C. Fung, K. Abe, H. Kumomi, and J. Kanicki, *IEEE J. Display Technol.* (in press).
- ⁴²M. C. Hamilton, S. Martin, and J. Kanicki, *Chem. Mater.* **16**, 4699 (2004).
- ⁴³R. L. Hoffman, *J. Appl. Phys.* **95**, 5813 (2004).
- ⁴⁴T. Kamiya, H. Hiramatsu, K. Nomura, and H. Hosono, *J. Electroceram.* **17**, 267 (2006).
- ⁴⁵H. Yabuta, M. Sano, K. Abe, T. Aiba, T. Den, H. Kumomi, K. Nomura, T. Kamiya, and H. Hosono, *Appl. Phys. Lett.* **89**, 112123 (2006).